# Microscopic Structure of Metal Whiskers

Vamsi Borra[*] and Daniel G. Georgiev[†]

*Department of Electrical Engineering and Computer Science,*
*University of Toledo, Toledo, Ohio 43606, USA*

V. G. Karpov[‡]

*Department of Physics and Astronomy, University of Toledo, Toledo Ohio 43606, USA*

Diana Shvydka[§]

*Department of Radiation Oncology, University of Toledo Health Science Campus,*
*Toledo, Ohio 43614, USA*

We present TEM images of the interior of metal whiskers (MWs) grown on electroplated Sn films. Along with earlier published information, our observations focus on a number of questions, such as, why MWs' diameters are in the micron range (significantly exceeding the typical nanosizes of nuclei in solids), why the diameters remain practically unchanged in the course of MW growth, what the nature of MW diameter stochasticity is, and what the origin of the well-known striation structure of MW side surfaces is. In an attempt to address such questions, we perform an in-depth study of MW structure at the nanoscale by detaching a MW from its original film, reducing its size to a thin slice by cutting its sides by a focused ion beam, and performing TEM on that structure. Also, we examine the root of the MW and Cu-Sn interface for the intermetallic compounds. Our TEM observations reveal a rich nontrivial morphology suggesting that MWs may consist of many side-by-side grown filaments. This structure appears to extend to the outside whisker surface and be the reason for the striation. In addition, we put forward a theory where nucleation of multiple thin metal needles results in micron-scale and larger MW diameters. This theory is developed in the average field approximation similar to the roughening transitions of metal surfaces. The theory also predicts MW nucleation barriers and other observed features.

## I. INTRODUCTION

The high-aspect-ratio (up to 10 000) metal filaments growing on surfaces of various metals and known as metal whiskers (MWs) cause significant reliability concerns in electronics. However, the nature of MWs is not sufficiently understood. Multiple outstanding questions include both factual and theoretical aspects. Comprehensive databases of information about tin and other metal whiskers are available through Internet resources [1,2]. Below, we mention only a few features.

MW concentrations are small compared to the surface concentration of grains (say, by a factor of $10^{-3}$–$10^{-5}$), varying exponentially between different local regions on the metal surface [3–8]; some of the nominally identical samples may exhibit no MWs, whereas others show significant MW infestations. Growing or eliminating

MWs "on demand" remains practically impossible, which aggravates the reliability concerns. Whisker heights ($10^{-4} \lesssim h \lesssim 1$ cm) and radii ($10^{-5} \lesssim R \lesssim 10^{-3}$ cm) are characterized by broad uncorrelated log-normal distributions [9–11]. It was established that material for MWs is supplied from the large areas far from MW locations [12]. A succinct summary of whisker properties was given by Davy [5].

While the mechanism behind metal whiskers remains mysterious, one hypothesis points at the mechanical stress relaxing during whisker growth and thus providing the necessary driving force [13–18]. Local recrystallization regions [19–21] and intermetallic compounds [17,22,23] have been referred to as possible stress sources. It was inferred also that the stress gradients can be more important than stresses itself [24–27]. Unfortunately, these approaches lack predictive power, providing no estimates for whisker growth rates and parameters.

A recent electrostatic theory [28–36] attributes MW driving forces to the electric fields, induced either by surface imperfections (charge patches) or externally.

[*]vamsi.borra@utoledo.edu
[†]daniel.georgiev@utoledo.edu
[‡]victor.karpov@utoledo.edu
[§]diana.shvydka@utoledo.edu

That theory predicts MW nucleation barrier, growth rates, and statistics of MW lengths vs certain material parameters, such as the surface tension $\sigma$ and surface charge density $n$. However, a number of important questions remain.

Here, we address two outstanding questions.

(1) Which factors are responsible for the characteristic MW diameters remaining almost the same in the process of longitudinal growth, and what determines their statistical distributions? We note that the MW thickness, which is in the micron range, is much greater than the nanosizes of the typical nuclei in solids.

(2) Can MWs have some internal structure at the nanoscale? It is motivated by the following observations: (i) the well-known longitudinal striations on MW surfaces (also illustrated in the pictures below); (ii) generally asymmetric randomly shaped whisker cross sections strongly deviating from the circular; furthermore, voids inside MWs have been reported [37,38]; (iii) and observations of split or branching whiskers showing separated filaments of diameters much smaller than that of the original whisker [39–41].

The methods and the nomenclature of magazines characteristic of the published whisker research show a surprisingly small contribution of physics. It may be partially due to that lack of attention that the 70-year old whisker challenge remains outstanding, unlike many developments in physics (e.g., superconductivity, which was discovered in 1911 and explained in 1957, in spite of being the first encounter with the macroscopic quantum world). Attracting attention from physics is another goal of this paper.

Our paper is organized as follows. In Sec. II, we present our FIB cross-sectioning work on tin whiskers along with SEM and transmission-electron-microscopy (TEM) imaging and other results, demonstrating evidence for rich morphology in the inner region of MWs that appears to be a combination of multiple nanofilaments grown side by side. A related theory presented in Sec. III shows indeed that, under certain realistic conditions, metal filaments can develop in the regime of massive nucleation leading to the multifilament MW structures. Our conclusions are summarized in Sec. IV.

## II. FOCUSED ION BEAM CROSS SECTIONING OF Sn WHISKER SAMPLES

Sn films with a thickness of about 500 nm are deposited on bulk Cu substrates by electroplating; see Ref. [11] for more details regarding the plating process. These Sn film samples are kept under normal lab environment conditions for several months to develop Sn whiskers, which are the subject of this FIB cross-sectioning and characterization study. Figure 1 shows a SEM image of the original Sn whisker that grew on the Cu substrate prior to the cross-section analysis. This whisker is then coated (with Pt as
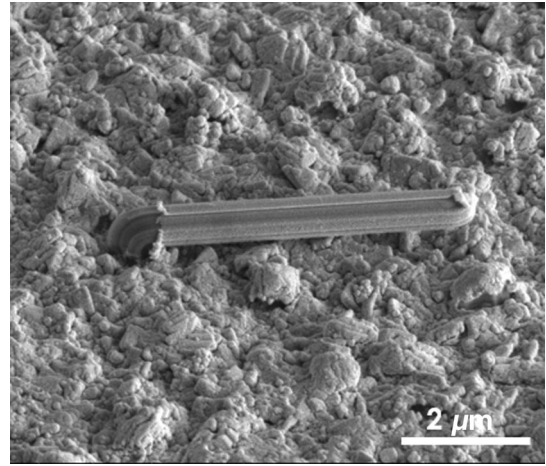


FIG. 1.   A SEM image of the original whisker before depositing platinum and performing the cross sectioning.

well as Pd and Au, which are commonly used in FIB sample processing) for protection, and then it is FIB milled to expose the material within the whisker, as well as in its immediate vicinity.

Figure 2 shows the standard SEM images [i.e., obtained using the secondary electrons in Fig. 2(b)] of the cross-sectioned whisker together with a backscattered electron image [Fig. 2(c)] and an ion-beam image [Fig. 2(a)] of the same sample. The last two imaging methods are more sensitive to chemical composition. They can be used to examine for possible intermetallic compounds (IMCs), with all three images serving as complementary tools for examining the sample chemistry and structure. From Figs. 2(a)–2(c), it is clear that the whisker consists of Sn material, and a very thin layer of oxide appears on its outside surface. It is worth noticing that, although Figs. 2(a) and 2(b) are the cross-section images obtained from the same original whisker (Fig. 1), Fig. 2(a) reveals greater detail regarding the Cu-Sn layer separation in the form of a contrast difference. More importantly, however, Figs. 2(a) and 2(c) and our other recent work [42] show no signs of IMCs, unlike some reports by other groups [43] that consider IMCs to be a major factor of whisker formation. While we do not see any signatures of IMCs, these results do not exclude some diffusion of small amounts of Cu into the Sn layer, which is generally possible even at room temperature.

Figures 3(a)–3(c) show the preparation stages of a Sn whisker cross-section sample for TEM imaging and analysis. TEM imaging requires a thin-enough sample (typically with a thickness of about 100 nm or less), so the whisker needs to be thinned on both sides to obtain, essentially, a slice of the whisker along its length or axis. In order to make the FIB work easier and to minimize the thinning time, a relatively straight and small-in-diameter whisker is chosen—shown in Fig. 3(a) with red arrows (this is another whisker that grows on an electroplated Sn film). Figure 3(b)
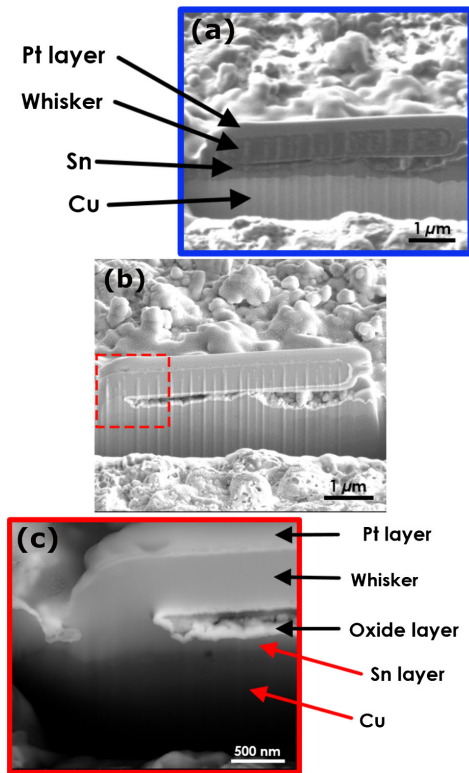
FIG. 2. (a) Secondary-ion image of the whisker cross section revealing greater detail on Cu-Sn separation in the form of contrast difference, whereas (b) the SEM image of the same area does not provide much information. The vertical beam lines in (b) result while we perform the cross section. (c) Close-up scan, which clearly shows the whisker under the Pt layer and the oxide layer on the whisker's surface, of the red highlighted box in (b) taken using a backscattered electron detector.

is the top view of the whisker [Fig. 3(a)] that is thinned down to an electron transparent thickness. The side view of Fig. 3(b), which is shown as Fig. 3(c), confirms that the structure of the original whisker [Fig. 3(a)] remains intact under the protective Pt layer and is not damaged by the ion beam during the mounting and thinning process.

Figure 4 shows a lower-magnification TEM image of the whole stack of the FIB machined and thinned sample [Fig. 3(c)], together with higher-magnification images of different parts of the whisker. In addition, a dark-field image [Fig. 4(d)] is shown which provides a different view of the whisker's internal morphology. One can clearly see lines oriented along the length or axis of the whisker that can be associated with filaments constituting its volume. While these images show evidence of more than just a longitudinal structure (i.e., there appears to be a fine-grained structure, which, perhaps, could be attributed to sample thickness variations and could be milling or thinning processing related), it is important to note that the longitudinal filament structure persists under both straight [Figs. 4(b) and 4(c)] and curved conditions [the kink in Fig. 4(d)]. Finally, in Fig. 4(e), we present a
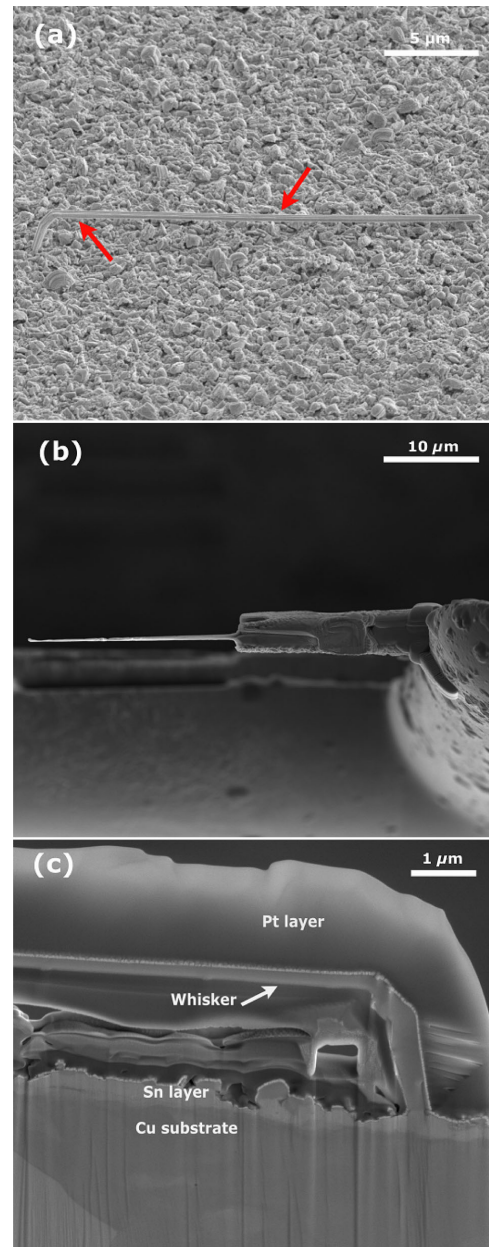


FIG. 3. (a) Original whisker selected for TEM analysis. (b) Top-view SEM image taken after thinning down to the elected transparent thickness. (c) Side view of the same sample shown in (b), in which the whisker remains undamaged under the protective Pt layer. Sn-Cu separation can also be seen.

selected-area electron diffraction (SAED) pattern taken from the volume of the whisker with a 50-nm-diameter $e$-beam. The spot pattern indicates well-aligned crystalline material within the whisker.

Line-scan and chemical mapping using energy-dispersive x-ray spectroscopy (EDS) analysis over the cross section of the sample is performed (see Fig. 5) to confirm the composition of the whisker. Figure 5 confirms the presence of only Sn across the diameter of the whisker, whereas Pt, Pd, and Au are present at its
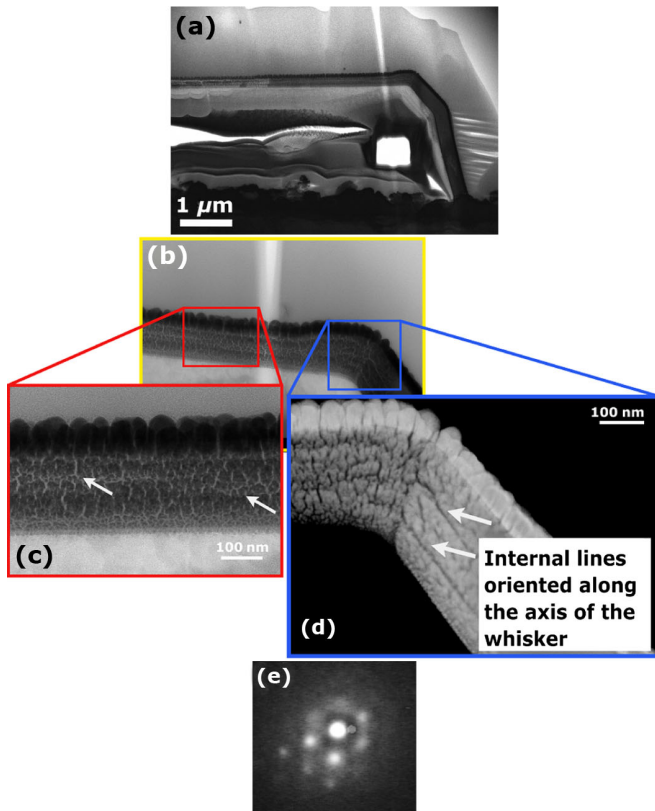
FIG. 4. (a) Lower-magnification TEM image of the whisker and surrounding material after FIB thinning. (b)–(d) Higher-magnification images exhibit greater detail regarding the internal structure and filament orientation along the axis of the whisker (indicated by arrows). (e) SAED pattern confirming the highly oriented crystalline structure.

surface. As mentioned above, Pt and Pd-Au coatings are used to protect the whisker from ion-induced damage during the FIB cross sectioning and thinning. In addition, the whisker's surface contains low amounts of oxygen, which is likely due to a minor level of oxidation of the whisker's outer surface. The arrow in the inset of Fig. 5 shows the line-scan direction along the diameter that starts at point 1 and extends to point 18. The results indicate that the bulk of the whisker consists of Sn, and no detectable amount of O or Cu (within the sensitivity of the method, which is about 5%) is found. The reason we specifically mention Cu is related to the possibility of significant Cu diffusion in the Sn film and in the whisker material itself.

Also, we perform x-ray diffraction (XRD) measurements (see Fig. 6) on the electroplated Sn films in order to examine the crystalline grain size of the original Sn film. JADE [44] analysis software (version 2010, Materials Data, Livermore, California) is used to perform the crystallite size calculations based on Williamson-Hall theory [45]. In the JADE size analysis [46], the pseudo-Voigt function is employed as a peak-shape function and broadening due to the crystalline size is isolated from the inherent instrument broadening by deconvolution. The results show a crystalline grain size of $67 \pm 23$ nm, which generally matches the apparent thickness of the internal filaments in Fig. 4.

We end this experimental section with the following conclusions.

(1) Our in-depth study of MW structure at the nanoscale is conducted by detaching a MW from the original film, reducing its size to a thin slice with a precisely controlled ion beam, and performing TEM on that structure.
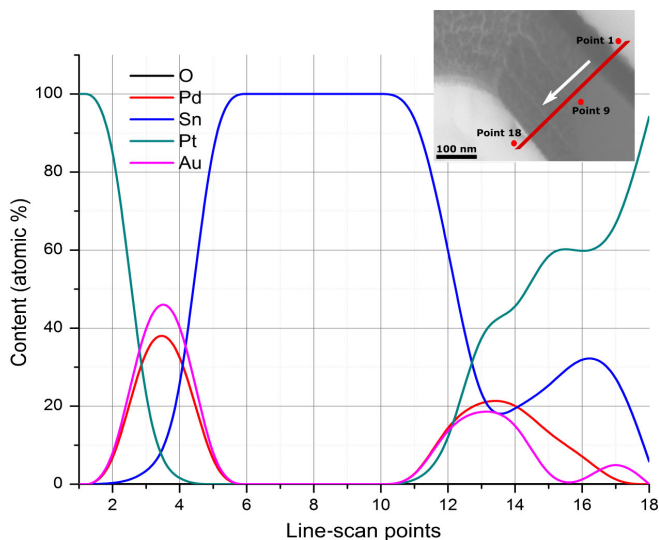


FIG. 5. Chemical composition information, obtained from EDS analysis over the complete cross section of a whisker. (Inset) Three out of eighteen EDS analysis points uniformly distributed along the straight line, from which the signal is taken. (The low oxygen level is not seen on the graph.)
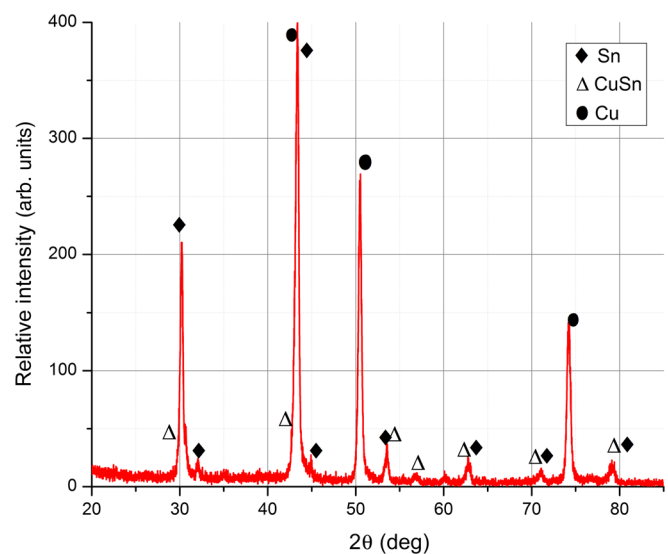


FIG. 6. An XRD pattern of electroplated Sn films on a Cu substrate.

(2) We verify that the structure of the original whisker remains intact under the protective Pt layer and is not damaged by the ion beam during the mounting and thinning process.

(3) EDS study at nanoscale reveals the chemical composition of Sn MWs coated with thin Au, Pd, and Pt layers.

(4) Examining the root of the MW and Cu-Sn interface, no evidence of intermetallic compounds is found.

(5) Our TEM observations reveal a rich nontrivial morphology suggesting that MWs may consist of many side-by-side-grown filaments. This structure appears to extend to the outside whisker surface and be the reason for the striation.

(6) The XRD estimates characteristic sizes of crystalline grains (in tens of nanometers) composing larger grains of the Sn film correlated with the diameters of the MWs forming thin filaments.

## III. MASSIVE NUCLEATION OF METAL FILAMENTS

Our consideration is based on the electrostatic theory [28,33,34], MWs grow due to the random electric field generated by charged surface imperfections, such as grain boundaries, contaminations, etc. The distribution of charges is presented by the uncorrelated charge patches of the characteristic dimension $L$, as illustrated in Fig. 7.

### A. Field-induced nucleation

Here, we briefly recall the concept of field-induced nucleation [28]. The field-induced electric dipole $p = \beta E$ decreases the energy of a needle-shaped metal filament by $-pE = -\beta E^2$. Because the polarizability [47] $\beta \sim h^3$ can be rather high while the surface area is small, filament nucleation and growth become possible. To the accuracy of insignificant numerical and logarithmically weak multipliers, the free energy can be written as
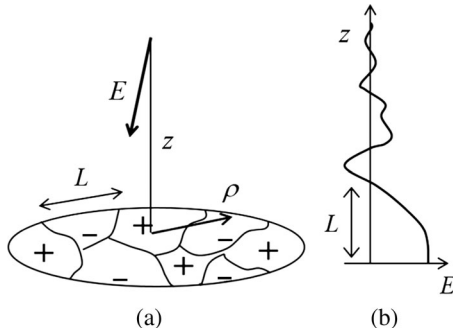


(a)                    (b)

FIG. 7. (a) A sketch of charge patches on a metal surface and their induced random electric field. (b) A sketch of the coordinate dependence of the random electric field vs the distance from a metal surface.

$$F = -E^2 h^3 + \sigma h R, \tag{1}$$

where the first and second terms represent, respectively, the electrostatic and surface contributions, $\sigma$ is the surface tension, $R$ is the filament radius, $h$ is its length, and $E$ is the normal component of the random electric field. The condition $\partial F/\partial h = 0$ yields the nucleation barrier and critical length, respectively,

$$W(E) = \sigma R \sqrt{\frac{\sigma R}{E^2}}, \qquad h \approx h_0(E) \equiv \sqrt{\frac{\sigma \Lambda R}{E^2}}. \tag{2}$$

Since $W$ is field dependent and the field is random, the nucleation times $\tau = \tau_0 \exp(W/kT)$, where $\tau_0 = \text{const}$, are distributed in the exponentially broad interval. Because $W$ increases with $R$, the smallest $R$ values are favorable, limited by extraneous requirements, such as, e.g., sufficient integrity. It has been estimated that a reasonable minimum diameter is in the subnanometer range [28].

The value of $\sigma$ in Eq. (2) depends on which type of surface is essential. For tin, the macroscopically averaged value [48–50] is $\sigma \sim 500$ dyn/cm, while the grain-boundary-related values can be as low as [51] $\sigma \sim 100$ dyn/cm, or even [52] $\sigma = 30$ dyn/cm. Along with the near-surface-field strength $E \sim 1$–10 MV/cm, the lowest reported value $\sigma = 30$ dyn/cm yields $W \sim 0.3$–10 eV and $h_0 \sim 2$–20 nm, which are in the ballpark of nucleation barriers known for various processes.

The postnucleation growth rate of a metal filament in a random electric field has been shown to be constant in time, on average [28]. When the filament tip enters a random low-field region, its growth ceases either temporarily [35] or terminally determining the stationary length distribution [33]. However, the question of filament diameter distribution has not been sufficiently answered.

Furthermore, the average radius evolution described by the Fokker-Planck's type of equation [28],

$$\frac{dR}{dt} = -b \frac{\partial F}{\partial R}, \tag{3}$$

where $b$ is the mobility in the radius space and $t$ is time, does not predict radial growth. Indeed, using $F$ from Eq. (1) with $E = \text{const}$ shows that the growth condition $dR/dt > 0$ requires $R < h^2 E^2/\sigma$. Because the latter value is in the subnanometer range, one concludes that the originally nucleated nanometer-radius filament will not grow because it is suppressed by the surface energy loss.

We end this subsection by noting one important feature of the above-described needle-shaped filaments: they suppress the original electric field in the proximity of their lengths $h$, thus suppressing the field-induced nucleation of other particles. Such a negative feedback makes the filament radial growth even less likely.
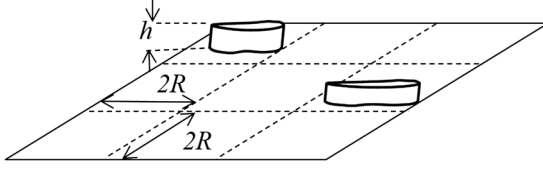
FIG. 8. A model of metal whiskers in a limited surface area divided into domains of the average linear dimension $2R$, with each accommodating a whisker.

## B. Massive nucleation and MW formation

Here, we consider an alternative scenario of field-induced nucleation illustrated in Fig. 8 where metal "pancakes" with a small aspect ratio, $h/R \ll 1$, can nucleate side by side and coalesce, forming an integral entity with a diameter in the micron range. Such a scenario leads to the multifilament microscopic whisker structure of the type presented in Fig. 4.

According to that scenario, the transversal geometrical dimensions, i.e., a MW cross-section shape is determined by that of the original charge patch, giving rise to the MW or an individual grain underlying the MW. Because of the charge patches and the grain asymmetric shapes, one should expect not a circular cylinder but rather some irregular cross sections, which is consistent with multiple published observations, as well as those in Figs. 3 and 4. Such irregular shapes can even include hollow MWs, in which the hollowness is inherited from the corresponding charge patch distribution. Furthermore, the skeleton of individual thin needle-shaped particles can exhibit itself in the peripheral region rending the typically observed longitudinal MW striations reflected, as well in Figs. 3 and 4.

To consider the above scenario more quantitatively, we assign the area $R^2$ to each of the many whiskers formed in a surface of area $A$, representing a charge patch, as illustrated in Fig. 8. Because of the irregular shapes of individual MWs, we do not discriminate between a MW cross-section area and that of a square cell. Similarly, to the accuracy of a numerical multiplier, the MW side-surface energy is estimated as $\sigma h R$. The total number of MWs in area $A$ is given by $(A/R^2)\delta$, where $\delta$ is the dimensionless MW concentration.

A single whisker's energy is similar to that in Eq. (1),

$$F_R = -E^2 h R^2 + \sigma h R. \qquad (4)$$

Here, the first term represents the "flat plate capacitor energy" gained due to its discharge related to the metal occupying the former field region (and the multiplier $\Lambda$ is irrelevant). In the average field approximation, the energy of filament pair interactions are accounted for by the multiplier $(1 - \delta)$ in front of $\sigma$, reflecting the decrease in surface energy when two filaments nucleate side by side. That approximation follows the average field theory of the metal surface roughening transition [53,54], with the

difference that, here, the cell size $2R$ is the (yet unknown) filament diameter, instead of the interatomic distance. Adding also the entropy contribution, $kT(A/R^2)[\delta \ln \delta + (1 - \delta) \ln(1 - \delta)]$, the free energy of a domain of area $A$ possessing the dimensionless MW concentration $\delta$ can be presented in the form

$$
\begin{aligned}
F = AhE^2 \{ & x\delta(1 - \delta) - \delta \\
& + \alpha x^2 [\delta \ln \delta + (1 - \delta) \ln(1 - \delta)] \}.
\end{aligned} \qquad (5)
$$

Here,

$$x \equiv \frac{\sigma}{E^2 R} \equiv \frac{R_E}{R} \quad \text{and} \quad \alpha \equiv \frac{kTE^2}{\sigma^2 h}. \qquad (6)$$

In Eq. (5) the energy gain is attributed to suppression of the electrostatic field and the energy inside it. That takes place when the pancake height $h$ is greater than the screening length $h_s$ in a metal; typically, $h_s \sim 3$ Å. Given the latter limitation, one gets $\alpha \ll 1$ for any practically possible parameters in Eq. (6). We estimate another characteristic quantity $R_E = \sigma/E^2$ by assuming the above-mentioned $E = 1$–10 MV/cm and $\sigma = 30$–500 dyn/cm, which yields $R_E \sim 5$–500 nm. We note that the microfilament diameters in Fig. 4 fall in the last range.

A nontrivial feature of the free energy in Eq. (5) is that it neglects the material volume conservation in the charge patch region of area $A$, thereby assuming material influx from the outside region of a much lower surface charge density and field strength. Indeed, assuming the opposite, i.e., the volume conserved in the patch region, growing the pancakes depresses the rest of the area, leaving the total volume occupied by the uniform field and electrostatic energy the same. That balance eliminates the second term in Eq. (5), nullifying the energy gain. To the contrary, assuming that the pancake material is supplied from a remote low-field region destroys the leasing to the electrostatic energy gain. The last assumption is consistent with the earlier-mentioned fact that MW material diffuses long distances to MW locations [12].

The free energy of Eq. (5) is plotted in Fig. 9. The standard analysis shows that it has a saddle point and a maximum located, respectively, at $x_{SP} = 2$, $\delta_{SP} \approx 1 - \exp[-1/(4\alpha)]$ and $x_{\max} = 1/(8\alpha \ln 2)$, $\delta_{\max} \approx 0.5 - (16\alpha \ln 2)/3$.

As is seen from Fig. 9, the system free energy is a minimum at $x \to 0$, $\delta \to 1$ corresponding to a single filament occupying the entire area. That large-area filament can be identified with MWs. The red arrows in Fig. 9 illustrate the system pathways towards the single MW finale. As formed, such a MW can further increase its length (electric dipole) according to the above outlined standard electrostatic theory.

An alternative type of energy decrease represented by the black arrows in Fig. 9 leads to $\delta \to 1/2$ and $x \to \infty$, i.e., very thin MWs occupying 50% of the area. However, a
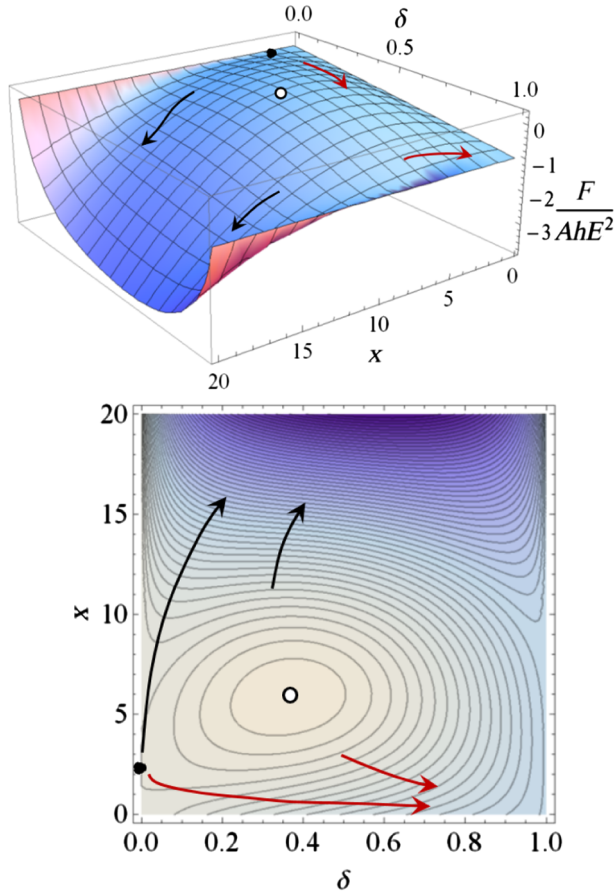
FIG. 9. (Top panel) The average field free energy of an ensemble of low-aspect-ratio filaments vs their relative concentration $\delta$ and reciprocal radius parameter $x$. The black and white marks represent, respectively, the saddle and maximum points. The red and black arrows illustrate, respectively, the pathways of system evolution towards two alternative scenarios: a single filament occupying the entire system area and multiple thin filaments that, in the approximation of Eq. (5), occupy half of the area ($\delta = 0.5$). (Bottom panel) Contour plot of the same.

large enough $x$ value ($\gg 1$) corresponds to a small radii $R$, and small-area filaments are inconsistent with the low-aspect-ratio model of Fig. 8 To more adequately describe this situation, one can modify the free energy to the form that utilizes the electrostatic of high-aspect-ratio filaments, $E^2 h^3 / \Lambda$ [see the discussion before Eq. (2)],

$$\frac{F}{Ah^2} = \sigma R h \delta - E^2 h^3 \delta (1 - \delta)$$
$$+ kT[\delta \ln \delta + (1 - \delta) \ln(1 - \delta)]. \quad (7)$$

Here, the second (electrostatic) term accounts for the effect of mutual filament suppression mentioned by the end of Sec. III A. The free energy of Eq. (7) is a minimum when

$$h = \sqrt{RR_0} \quad \text{and} \quad \delta = -\frac{kTE \ln \delta}{(\sigma R)^{3/2}}. \quad (8)$$

The last $h$ coincides with that in Eq. (2), and the dimensionless filament concentration is small, $\delta \ll 1$, for any practical parameters. We conclude that the massive nucleation of high-aspect-ratio filaments would result in rare nanometer thin needles.

Consider possible pathways leading to much-greater-than-nanometer-thick MWs. Because the coherent nucleation of multiple ($N \gg 1$) filaments is suppressed by the necessity to overcome large ($NW \gg W$) barriers, we assume that the filaments nucleate in random fashion, one after another. A single pancake nucleation barrier ($W_{Rn}$) and radius ($R_n$) are determined from Eq. (4),

$$W_{Rn} = \sigma R_0 h_s / 4 \quad \text{and} \quad R_n = R_E / 2, \quad (9)$$

where $h_s$ is the screening radius in a metal [see the discussion after Eq. (5)]. Because $x = R_E / R_n = 2$ and the pancake appearance starts with $\delta \ll 1$, we conclude that, in Fig. 9, the pancake nucleation takes place in a narrow proximity of the saddle point. Therefore, approximately equal fractions of filaments appear as small-aspect-ratio pancakes and high-aspect-ratio needles.

Because the latter entities remain in low concentration and do not grow their radii [see the discussion after Eq. (3)], they can be neglected as a possible source of MW development. To the contrary, it follows from Eq. (3), with the free energy from Eq. (4), that the pancake-shaped nuclei grow with time exponentially, $R \propto R_n \exp(\lambda t)$, with $\lambda \approx 2bE^2 h_s$. Eventually, they come to a physical contact with each other, forming a single MW ($\delta = 1$) that corresponds to the free-energy minimum. The last conclusion completes our scenario of the nucleation and growth of micron-thick MWs. This scenario explains the observations in Fig. 4.

We end this section with a comment regarding the grain and crystallite (within a grain) structure of a metal, in particular, the Sn films under consideration. One possible effect is that the original thin filaments will stop increasing their radii $R$ when the latter reach the crystallite size. In that case, one should expect MWs formed by a cojoint growth of the crystallite thick filaments. That possibility is consistent with the observations in Sec. II regarding the filament and crystallite diameters.

Second, when the cojoined MW grows to the diameter of its underlying grain, its further development can be inhibited by the grain-boundary effects (strongly affecting the field strength and surface tension). Should that be the case, the statistics of the measured MW diameters would coincide with that of the film grains. This conclusion calls upon additional experimental verification that will be presented elsewhere.

Finally, because the above scenario predicts the uncorrelated nucleation of MWs forming individual filaments, one can expect that, at any given instant, they will have somewhat unequal growth rates and corresponding longitudinal stresses, leading to multiple breaks in the

transversal directions. This prediction could explain the transversal grainlike features described in Sec. II.

## IV. CONCLUSIONS

Our FIB-facilitated TEM images exhibit a rich internal morphology of tin whiskers, pointing at their composite structure. The whiskers consist of multiple filaments whose individual radii are in the range of tens of nanometers. The universality of that conclusion remains to be verified by performing similar analyses on other types of Sn films, as well as on other metal films (Zn, Ag, Cd, etc.) known for their whisker propensity. (We recall that a microfilamentary structure of metal whiskers in other systems has been observed, but not systematically studied [39–41].)

At this time, the electrostatic concept appears to be the only theoretical framework capable of explaining our observations. In particular, it predicts filament radii consistent with the measurements.

The scenario of massive filament nucleation put forward in this work explains as well some earlier-established facts, such as the geometrically irregular shapes of metal whiskers, observations of hollow and branching whiskers, their characteristic diameters, and why long-distance lateral diffusion is needed to form MWs.

Simultaneously, this theory calls upon a variety of follow-up work that can have practical significance, such as a possible correlation between the individual filament diameters and crystallite sizes. For example, the filament nucleation would be suppressed if the crystallite sizes were smaller than the nucleation radius. Similarly, verifying the above-predicted correspondence between MW and grain diameters would pave the way to MW mitigation by affecting the grain diameter distribution through properly chosen film deposition parameters.

## ACKNOWLEDGMENTS

[1] NASA Goddard Space Flight Center Tin Whisker website, http://nepp.nasa.gov/whisker.

[2] J. R. Barnes, Bibliography for tin whiskers, zinc whiskers, cadmium whiskers, indium whiskers, and other conductive metal and semiconductor whiskers, http://www.dbicorporation.com/whiskbib.htm.

[3] G. T. Galyon, Annotated tin whisker bibliography and anthology, IEEE Trans. Electron. Packag. Manuf. **28,** 94 (2005); http://thor.inemi.org/webdownload/newsroom/TW_biblio-July03.pdf.

[4] J. Brusse, G. Ewell, and J. Siplon, *Tin whiskers: Attributes and mitigation, in Proceedings of the Capacitor and Resistor Technology Symposium (CARTS) 2002: 16th Passive Components Symposium, Nice, France, 2002* (Huntsville, AL, 2002), p. 68.

[5] G. Davy (private communication), quoted in Ref. [29].

[6] Y. Zhang, Tin whisker discovery and research, in *Soldering in Electronics*, edited by K. Suganuma (Marcel Dekker, New York, 2004), p. 121.

[7] K. N. Tu, J. O. Suh, and Albert T. Wu, Tin whisker growth on lead-free solder finishes, in *Lead-Free Solder Interconnect Reliability*, edited by D. Shangguan (ASM International, Materials Park, OH, 2005), p. 851.

[8] D. Bunyan, M. A. Ashworth, G. D. Wilcox, R. L. Higginson, R. J. Heath, and C. Liu, Tin whisker growth from electroplated finishes a review, Trans. Inst. Met. Finish. **91,** 249 (2013).

[9] T. Fang, M. Osterman, and M. Pecht, Statistical analysis of tin whisker growth, Microelectron. Reliab. **46,** 846 (2006).

[10] L. Panashchenko, master's thesis, University of Maryland, 2009, http://hdl.handle.net/1903/10021.

[11] D. Susan, J. Michael, R. P. Grant, B. McKenzie, and W. G. Yelton, Morphology and growth kinetics of straight and kinked tin whiskers, Metall. Mater. Trans. A **44,** 1485 (2013).

[12] T. A. Woodrow, Tracer diffusion in whisker-prone tin platings, in *Proceedings of the SMTA International Conference, Rosemont, IL, 2006* (Surface Mount Technology Association (SMTA), Red Hook, NY, 2007), pp. 1–50, https://nepp.nasa.gov/whisker/reference/tech_papers/2006-Woodrow-Paper-Tin-Tracer-Diffusion.pdf.

[13] F. Pei and E. Chason, *In situ* measurement of stress and whisker/hillock density during thermal cycling of Sn layers, J. Electron. Mater. **43,** 80 (2014).

[14] E. Chason, F. Pei, C. L. Briant, H. Kesari, and A. F. Bower, Significance of nucleation kinetics in Sn whisker formation, J. Electron. Mater. **43,** 4435 (2014).

[15] F. Pei, C. L. Briant, H. Kesari, A. F. Bower, and E. Chason, Kinetics of Sn whisker nucleation using thermally induced stress, Scr. Mater. **93,** 16 (2014).

[16] W. J. Boettinger, C. E. Johnson, L. A. Bendersky, K.-W. Moon, M. E. Williams, and G. R. Stafford, Whisker and hillock formation on Sn, Sn-Cu and Sn-Pb electrodeposits, Acta Mater. **53,** 5033 (2005).

[17] N. Jadhav, E. J. Buchovecky, L. Reinbold, S. Kumar, A. F. Bower, and E. Chason, Understanding the correlation between intermetallic growth, stress evolution, and Sn whisker nucleation, IEEE Trans. Electron. Packag. Manuf. **33,** 183 (2010).

[18] P. Sarobol, J. E. Blendell, and C. A. Handwerker, Whisker and hillock growth via coupled localized Coble creep, grain boundary sliding, and shear induced grain boundary migration, Acta Mater. **61,** 1991 (2013).

[19] J. Cheng, P. T. Vianco, B. Zhang, and J. C. M. Li, Nucleation and growth of tin whiskers, Appl. Phys. Lett. **98,** 241910 (2011).

[20] P. Vianco, M. Neilsen, J. Rejent, and R. Grant, Validation of the dynamic recrystallization (DRX) mechanism for whisker and hillock growth on Sn thin films, J. Electron. Mater. **44,** 4012 (2015).

[21] L. Qiang and Z. Huang, A physical model and analysis for whisker growth caused by chemical intermetallic reaction, Microelectron. Reliab. **54,** 2494 (2014).

[22] K. N. Tu, Irreversible processes of spontaneous whisker growth in bimetallic Cu-Sn thin-film reactions, Phys. Rev. B 49, 2030 (1994).

[23] A. C. K. So and Y. C. Chan, Reliability studies of surface mount solder joints effect of Cu-Sn intermetallic compounds, IEEE Trans. Compon., Packag., Manuf. Technol., Part B 19, 661 (1996).

[24] J. Stein, M. Pascher, U. Welzel, W. Huegel, and E. J. Mittemeijer, Imposition of defined states of stress on thin films by a wafer-curvature method: Validation and application to aging Sn films, Thin Solid Films 568, 52 (2014).

[25] F. Yang and Y. Li, Indentation-induced tin whiskers on electroplated tin coatings, J. Appl. Phys. 104, 113512 (2008).

[26] M. Sobiech, U. Welzel, E. J. Mittemeijer, W. Hugel, and A. Seekamp, Appl. Phys. Lett. 93, 011906 (2008).

[27] M. Sobiech, M. Wohlschlgel, U. Welzel, E. J. Mittemeijer, W. Hugel, A. Seekamp, W. Liu, and G. E. Ice, Local, submicron, strain gradients as the cause of Sn whisker growth, Appl. Phys. Lett. 94, 221901 (2009).

[28] V. G. Karpov, Electrostatic Theory of Metal Whiskers, Phys. Rev. Applied 1, 044001 (2014).

[29] V. G. Karpov, Electrostatic mechanism of nucleation and growth of metal whiskers, SMT Mag. 30, 28 (2015), http://iconnect007.uberflip.com/i/455818/44.

[30] V. G. Karpov, Understanding the movements of metal whiskers, J. Appl. Phys. 117, 235303 (2015).

[31] A. C. Vasko, G. R. Warrell, E. I. Parsai, V. G. Karpov, and Diana Shvydka, Electron beam induced growth of tin whiskers, J. Appl. Phys. 118, 125301 (2015).

[32] A. C. Vasko, C. R. Grice, A. D. Kostic, and V. G. Karpov, Evidence of electric-field-accelerated growth of tin whiskers, MRS Commun. 5, 619 (2015).

[33] D. Niraula and V. G. Karpov, The probabilistic distribution of metal whisker lengths, J. Appl. Phys. 118, 205301 (2015).

[34] Diana Shvydka and V. G. Karpov, Surface parameters determining a metal propensity for whiskers, J. Appl. Phys. 119, 085301 (2016).

[35] B. Subedi, D. Niraula, and V. G. Karpov, The stochastic growth of metal whiskers, Appl. Phys. Lett. 110, 251604 (2017).

[36] M. Killefer, V. Borra, A. Al-Bayati, D. G. Georgiev, V. G. Karpov, E. I. Parsai, and D. Shvydka, Whisker growth on Sn thin film accelerated under gamma-ray induced electric field, J. Phys. D 50, 405302 (2017).

[37] H. Kehrer and H. Kadereit, Tracer experiments on the growth of tin whiskers, Appl. Phys. Lett. 16, 411 (1970).

[38] J. Cheng, P. T. Vianco, and J. C. M. Li, Hollow tin/chromium whiskers, Appl. Phys. Lett. 96, 184102 (2010).

[39] B. Rollins and S. Smith (private communication).

[40] J. Brusse (private communication).

[41] Y. Liu, P. Zhang, C. Ling, J. Ding, W. B. Tian, Y. M. Zhang, and Z. M. Sun, Spontaneous Sn whisker formation on Ti$_2$SnC, J. Mater. Sci. Mater. Electron. 28, 5788 (2017).

[42] V. Borra, S. Itapu, and D. G. Georgiev, Sn whisker growth mitigation by using NiO sublayers., J. Phys. D 50, 475309 (2017).

[43] E. Chason, N. Jadhav, F. Pei, E. Buchovecky, and A. Bower, Growth of whiskers from Sn surfaces: Driving forces and growth mechanisms, Prog. Surf. Sci. 88, 103 (2013).

[44] JADE, a program for powder diffraction data analysis, Materials Design, Inc., Livermore, CA, https://materialsdata.com/prodjd.html.

[45] G. K. Williamson and W. H. Hall, X-ray line broadening from filed aluminium and wolfram, Acta Metall. 1, 22 (1953).

[46] S. A. Speakman (MIT Center for Materials Science and Engineering), Estimating crystallite size using XRD, http://prism.mit.edu/XRAY/oldsite/CrystalSizeAnalysis.pdf (2014).

[47] L. D. Landau and E. M. Lifsitz, Electrodynamics of Continuous Media (Pergamon, Oxford, 1984).

[48] B. B. Alchagirov, O. I. Kurshev, and T.M Taova, Surface tension of tin and its alloys with lead, Russ. J. Phys. Chem. A 81, 1281 (2007).

[49] C. M. Rice, master's thesis, Missouri School of Mines and Metallurgy, 1949.

[50] I. Kaban, S. Mhiaoui, W. Hoyer, and J.-G. Gasser, Surface tension and density of binary lead and lead-free Sn-based solders, J. Phys. Condens. Matter 17, 7867 (2005).

[51] K. T. Aust and B. Chalmers, The specific energy of crystal boundaries in tin, Proc. R. Soc. A 204, 359 (1950).

[52] H. Saka, Y. Nishikawa, and T. Imura, Melting temperature of In particles embedded in an Al matrix, Philos. Mag. A 57, 895 (1988).

[53] Y. Saito, Statistical Physics of Crystal Growth (World Scientific, London, 1998).

[54] A. Pimpinelly and J. Villian, Physics of Crystal Growth (Cambridge University Press, Cambridge, England, 1998).